Scalar mixing in a Kelvin-Helmholtz shear layer and implications for Reynolds-averaged Navier-Stokes modeling of mixing layers

Brandon E. Morgan

Lawrence Livermore National Laboratory, Livermore, California 94550, USA

Large-eddy simulation of a temporally evolving Kelvin-Helmholtz (KH) mixing layer is performed with the tenth-order compact difference code MIRANDA to examine the steady-state behavior of a passive scalar in a shear-driven mixing layer. It is shown that the integral behavior of scalar variance in a KH mixing layer behaves similarly to the integral behavior of scalar variance in a Rayleigh-Taylor (RT) mixing layer, and mixedness of the simulated KH shear layer tends towards a value of about 0.8. It is further shown that if the *k-L-a-V* Reynolds-averaged Navier-Stokes (RANS) model [B. E. Morgan *et al.*, Phys. Rev. E **98**, 033111 (2018)], calibrated to reproduce steady-state mixing in an RT layer, is applied to simulate a KH mixing layer, the RANS model will significantly overpredict the magnitude of scalar variance in the KH layer. A straightforward addition to the *k-L-a-V* model is then suggested, and self-similarity analysis is applied to determine constraints on model coefficients. It is shown that with the addition of a buoyancy production term in the model equation for scalar variance, it becomes possible to eliminate the model deficiency and match steady-state mixedness in simulations of both RT and KH mixing layers with a single model calibration.

I. INTRODUCTION

The behavior of turbulent mixing layers is important to the understanding of a variety of physical systems including supersonic combustion [1], oceanic and atmospheric flows [2–5], astrophysical phenomena [6], and inertial confinement fusion (ICF) [7,8]. Within the ICF community, most historical explorations of the impact of turbulent mixing have focused on buoyancy- and shock-driven instabilities such as Rayleigh-Taylor (RT) and Richtmyer-Meshkov (RM) instabilities [9–15]. More recently, there has been increasing interest in the impact of shear-driven mixing in high-energy-density systems [16–21] which can be seeded by sources of asymmetry such as fill tubes, capsule supports, and x-ray shadowing [22–26]. Canonical Kelvin-Helmholtz (KH) instability is a shear-driven instability mechanism that occurs between two fluid streams with different parallel components of velocity [27,28]. In ICF applications, for instance, it is expected that when a shock interacts with a material interface obliquely, the normal component should contribute to RM instability while the parallel component should contribute to KH instability. Studying KH instability in isolation represents a simplified representation of the fundamental shear-driven mixing process that occurs in complex flows.

Since Reynolds-averaged Navier-Stokes (RANS) modeling remains a common tool for the design and analysis of ICF targets, the development and improvement of RANS models for variable density mixing remains a problem of significant interest, and a wide body of work has been devoted to this topic over the years [29–53]. Recently, the two-length-scale *k-L-a-V* (*k-2L-a-V*) model [42–44] has been developed for the simulation of reacting buoyancy-driven mixing layers.

Using self-similarity analysis, Morgan *et al.* [43] have determined constraints on model coefficients that, when satisfied, recover the expected steady-state *mixedness* for a Rayleigh-Taylor mixing layer, where the mixedness is defined by

$$\Theta \equiv 1 - \frac{\int_\infty^\infty \widetilde{Y_H'' Y_H''} dz}{\int_\infty^\infty \widetilde{Y_H} \widetilde{Y_L} dz} = 1 - \frac{\int_\infty^\infty V dz}{\int_\infty^\infty \widetilde{Y_H} \widetilde{Y_L} dz}. \quad (1)$$

In Eq. (1), Y_H and Y_L indicate the mass fraction of the heavy and light species, respectively, V indicates the model variable representing scalar variance, and the tilde indicates the mass-weighted Favre average such that an arbitrary scalar f is decomposed according to

$$f = \widetilde{f} + f''. \quad (2)$$

Given the importance of shear-driven mixing in ICF applications, it is desirable to evaluate and extend the *k-2L-a-V* model for problems of reacting shear-driven mixing. Before this can be achieved, however, it is first necessary to understand the steady-state behavior of scalar variance in a KH mixing layer. While there have been many previous studies of mechanical turbulence behavior and the transition to turbulence in a KH shear layer [54–64], fewer studies have focused on the behavior of a passive scalar [65–69]. Among those studies that have examined scalar mixing in a KH layer, fewer still have achieved sufficient development length, or time integration in the case of a temporal shear layer, to characterize late-time self-similar behavior. Thus, the present work is organized around two objectives. First, high-fidelity large-eddy simulation (LES) is conducted of a temporally evolving, incompressible KH mixing layer in which a passive tracer is transported by one fluid stream. This LES is evolved

until late time in order to gain an understanding of the self-similar mixedness of a KH mixing layer. Next the k-$2L$-a-V RANS model is applied to quasi-one-dimensional (quasi-1D) simulation of the same mixing layer, and improvements are presented that are necessary to allow the model to match both the steady-state mixedness of an RT mixing layer and the steady-state mixedness of a KH mixing layer.

The remainder of this work is laid out as follows. First, in Secs. II A and II B, a description is given of the MIRANDA code as well as the computational setup for LES of a temporally evolving KH mixing layer. Large-eddy simulation results are presented and discussed in Sec. II C with a focus on the late-time mixedness and profiles of scalar fluxes. Next, in Secs. III A–III C, the k-$2L$-a-V RANS model is presented along with similarity analysis for a steady-state shear layer and a description of the problem setup for quasi-1D RANS simulation of the temporally evolving mixing layer. Results of these simulations are presented in Sec. III D, and comparisons are made with LES. Finally, in Sec. IV, conclusions are drawn and recommendations are made concerning the direction of future research.

II. LARGE-EDDY SIMULATION OF A KH MIXING LAYER

A. The MIRANDA code

The code used to perform LES calculations in the present study is MIRANDA, a tenth-order compact finite-difference code developed at Lawrence Livermore National Laboratory. To maximize efficiency of computational resources, MIRANDA's incompressible formulation is utilized [70], which has been previously applied in problems of RT mixing [71–73]. Under this formulation, the governing equations for two incompressible, nonreacting, miscible fluids are given by

$$\frac{\partial \rho}{\partial t} + u_j \frac{\partial \rho}{\partial x_j} = -\rho \frac{\partial u_j}{\partial x_j} = \rho \frac{\partial}{\partial x_j}\left(\frac{D}{\rho}\frac{\partial \rho}{\partial x_j}\right), \quad (3)$$

$$\frac{\partial \rho u_i}{\partial t} + \frac{\partial \rho u_i u_j}{\partial x_j} = -\frac{\partial p}{\partial x_i} + \frac{\partial \tau_{ij}}{\partial x_j}, \quad (4)$$

where

$$\tau_{ij} = \mu\left(\frac{\partial u_i}{\partial x_j} + \frac{\partial u_j}{\partial x_i} - \frac{2}{3}\delta_{ij}\frac{\partial u_k}{\partial x_k}\right). \quad (5)$$

In Eqs. (3)–(5), ρ is the mixture density, u_j is the velocity vector, x_j is the spatial vector, D is the binary species diffusivity, p is the pressure, τ_{ij} is the viscous stress tensor, μ is the shear viscosity, and δ_{ij} is the Kronecker delta. For the present work, we notionally identify the fluid stream with greater velocity as fluid 2 and set the density of both fluid streams to the same value such that $\rho_1 = \rho_2$. Thus, the mass fraction of either fluid can be treated as a passive scalar. Without loss of generality, when discussing the behavior of a general scalar Y in the following sections, the scalar under consideration is the field associated with fluid 2.

Equations (3) and (4) are solved with a tenth-order compact difference scheme for spatial discretization and a fourth-order explicit Runge-Kutta scheme for temporal integration. A Poisson equation is solved to obtain the pressure gradient in Eq. (4). The Poisson solver utilizes a pseudospectral formulation, with an eighth-order compact stencil used for

second-derivative components in nonperiodic dimensions and spectral differentiation used with fast Fourier transform in periodic dimensions [74]. Additionally, MIRANDA utilizes an artificial fluid LES approach in which artificial transport terms are added to the fluid viscosity and diffusivity [75,76]. This formulation is given by

$$\mu = \mu_f + \mu^*, \quad (6)$$

$$D = D_f + D^*, \quad (7)$$

where the subscript f denotes the fluid, or physical, contribution and an asterisk superscript denotes the artificial contribution. The form of the artificial contributions used in the present study is the same as that used by Morgan and Black [73] in earlier simulations of RT mixing.

B. Problem setup and initial conditions

Simulations are conducted on a computational mesh of dimension $2\pi \times 2\pi \times 4\pi$ cm^3 with the streamwise dimension in x. The slower moving fluid stream is initialized such that the streamwise velocity $u = U_1 = 900$ cm/s for $-2\pi \leqslant z < 0$ and $u = U_2 = 1500$ cm/s for $0 \leqslant z \leqslant 2\pi$. This configuration corresponds to a shear-analog Atwood number $\mathcal{A} = 0.25$, where the shear-analog Atwood number is defined by

$$\mathcal{A} \equiv \frac{U_2 - U_1}{U_2 + U_1}. \quad (8)$$

Periodic boundary conditions are imposed in the x and y dimensions, and nonpenetrating slip-wall boundaries are imposed at $z = -2\pi$ and $z = 2\pi$. Constant mesh spacing is utilized in all dimensions such that the number of grid points in the z dimension, N_z, is equal to twice the number of grid points in the x and y dimensions, that is, $N_z = 2N_y = 2N_x$. Simulations are run until the integral mixing layer width $h_{\text{int}} = \pi$, where

$$h_{\text{int}} \equiv 4\int_{-2\pi}^{2\pi} \widetilde{Y}(1 - \widetilde{Y})dz. \quad (9)$$

To get an estimate of grid resolution requirements, it is useful to derive a relationship between the Kolmogorov length scale η and the grid Reynolds number defined by

$$\text{Re}_\Delta \equiv \frac{\Delta U \Delta_x}{\nu}. \quad (10)$$

In Eq. (10), ΔU indicates the velocity difference $U_2 - U_1$, Δ_x indicates the grid spacing, and ν indicates the kinematic viscosity. To arrive at a relationship between η and Re_Δ, consider that the specific dissipation rate ε can be related to a characteristic turbulence length scale l and turbulence kinetic energy k by

$$\varepsilon \sim \frac{k^{3/2}}{l}. \quad (11)$$

Thus, we can approximate the Kolmogorov length scale by

$$\eta = \left(\frac{\nu^3}{\varepsilon}\right)^{1/4} \approx \left(\frac{\nu^3 l}{k^{3/2}}\right)^{1/4}. \quad (12)$$

Recognizing for a fully developed mixing layer that $l \approx h_{\text{int}}$, defining the number of computational grid points across the

mixing layer as $N_h \equiv h_{\text{int}}/\Delta_x$, and substituting in Eq. (10), Eq. (12) can be rearranged to arrive at the expression

$$\frac{\eta}{\Delta_x} \approx \left(\frac{k}{(\Delta U)^2}\right)^{-3/8} \left(\frac{N_h^3}{\text{Re}_\Delta^3}\right)^{1/4}. \quad (13)$$

From experimental observations [56], the turbulence intensity $k/(\Delta U)^2$ is expected to reach a maximum value of about 0.035 along the center plane of the mixing layer. Thus, Eq. (13) can be simplified further,

$$\frac{\eta}{\Delta_x} \approx 3.52 \left(\frac{N_h^3}{\text{Re}_\Delta^3}\right)^{1/4}. \quad (14)$$

Using Eq. (14) as an *a priori* estimate, we select ν to fix $\text{Re}_\Delta = 100$ and use constant D_f corresponding to a Schmidt number of unity. Grid size is selected such that $N_z = 2048$, for a total of about 2.15×10^9 grid points. With an initial ten points across the mixing layer, it is therefore estimated that η/Δ_x should range between about 0.20 and 0.53 throughout the simulation. The simulation is therefore expected to be in the well-resolved LES regime with resolution extending into the dissipation range for the late-time, fully developed mixing layer [77].

Finally, an initial perturbation to the interface is specified in Fourier space as a function of the maximal and minimal wave numbers κ_{max} and κ_{min} according to

$$\xi(x, y) = \sum_{j=\kappa_{\text{min}}}^{\kappa_{\text{max}}} \sum_{k=\kappa_{\text{min}}}^{\kappa_{\text{max}}} \frac{\Delta_x}{\kappa_{\text{max}} - \kappa_{\text{min}} + 1} \cos(jx + \phi_{x,j})$$
$$\times \sin(ky + \phi_{y,k}), \quad (15)$$

where the phase shift vectors $\phi_{x,j}$ and $\phi_{y,k}$ are drawn from uniformly distributed random numbers between 0 and 2π. The streamwise velocity field at time $t = 0$ is then given by

$$u(x, y, z) = U_1 + \frac{\Delta U}{2}\left[1 + \tanh\left(\frac{z - \xi(x, y)}{5\Delta_x}\right)\right]. \quad (16)$$

An initial perturbation spectrum is selected such that $\kappa_{\text{min}} = 8$ and $\kappa_{\text{max}} = N_z/32$. Note that since the perturbation is only applied to the streamwise velocity component, the initial velocity field is expected to have nonzero divergence. A consequence of this discrepancy is likely the presence of spurious pressure waves at early time as the velocity field relaxes to a state of zero divergence.

C. Results and discussion

As discussed previously, the primary motivation of the LES portion of the present study is to gain some understanding of the late-time self-similar behavior of scalar mixing in a KH mixing layer. Figure 1 gives a qualitative impression of the mixing layer development by plotting contours of the scalar field at several time instants, where characteristic length scales and timescales have been defined according to

$$l_0 = \frac{4\pi}{\kappa_{\text{max}} + \kappa_{\text{min}}} \quad (17)$$

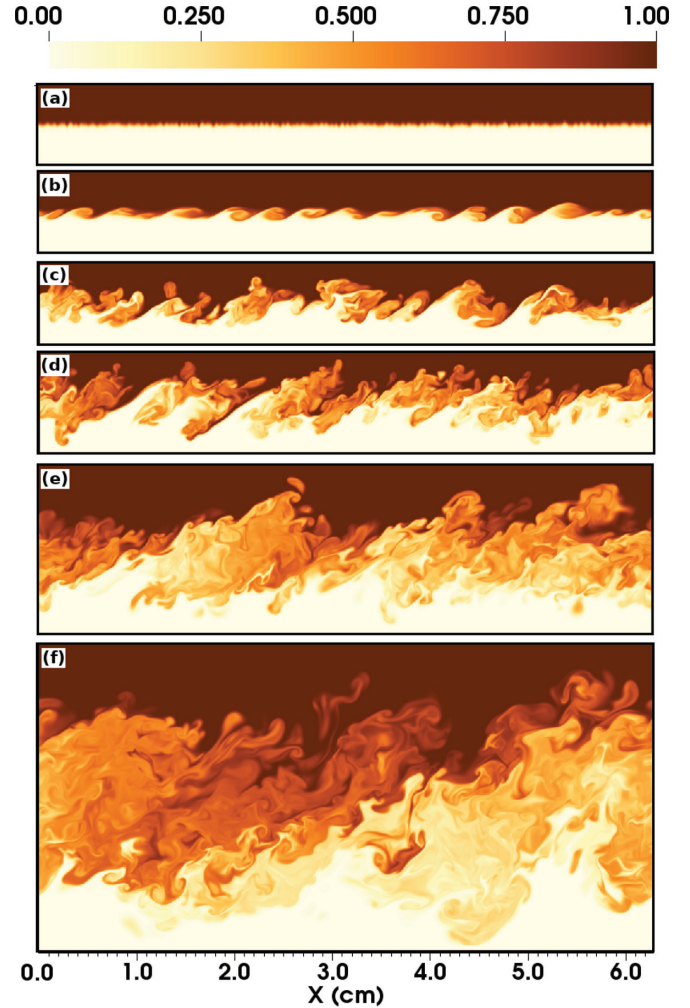and

$$t_0 = \frac{l_0}{\Delta U}. \quad (18)$$

FIG. 1. Slice of instantaneous Y contours in the $y = \pi$ plane taken at several times: (a) $t/t_0 = 0$, (b) $t/t_0 = 23.9$, (c) $t/t_0 = 43.6$, (d) $t/t_0 = 62.2$, (e) $t/t_0 = 119.3$, and (f) $t/t_0 = 340$.

Before examining the behavior of the scalar field, however, it is first necessary to examine the mechanical evolution of the mixing layer to identify the onset of steady-state behavior and to evaluate quality of the simulation against expected behavior. Figure 2(a) plots the temporal evolution of three measures of the mixing layer width as a function of time. In this figure, $h_{u,99}$ and $h_{Y,99}$ are defined as the distances between the 99% and 1% contours of velocity and the scalar fields, respectively, while h_{int} was defined previously by Eq. (9). Figure 2(b) plots the temporal evolution of the nondimensional growth parameter $\delta/\mathcal{A}$ derived from each of the three measures of mixing layer width, where for a given h, δ is the growth rate of a spatially developing mixing layer,

$$\delta \equiv \frac{dh}{dx}. \quad (19)$$

Thus, for a temporally evolving mixing layer, we have

$$\dot{h} = \frac{dh}{dx}\frac{dx}{dt} = \delta U_c, \quad (20)$$

where the dot notation has been used to indicate differentiation with respect to time and $U_c \equiv (U_2 + U_1)/2$ is the
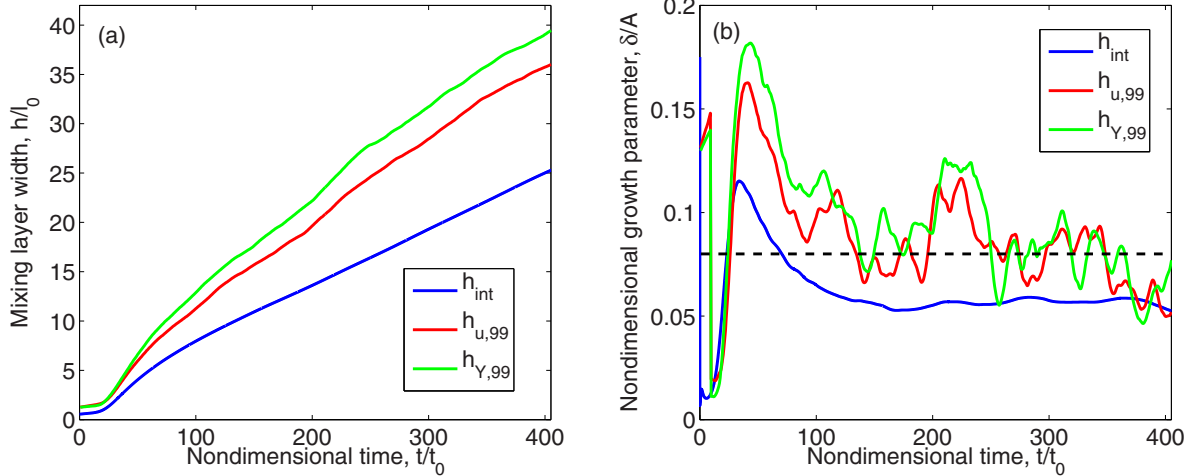
FIG. 2. Temporal evolution of three measures of mixing layer width: (a) mixing layer width as a function of time and (b) nondimensional growth parameter $\delta/\mathcal{A}$ as a function of time.

convective velocity. Thus, rearranging, we can write

$$\frac{\delta}{\mathcal{A}} = \frac{2\dot{h}}{\Delta U}. \tag{21}$$

From experimental observation, it is expected that the nondimensional growth parameter defined by Eq. (21) should reach a steady-state value around 0.08 [56]. Figure 2(a) shows that the mixing layer grows fairly linearly for $t/t_0 \gtrsim 100$, with $h_{u,99}$ and $h_{Y,99}$ taking a slightly greater value and demonstrating somewhat more oscillation than the integral mixing width. Figure 2(b) illustrates that for $t/t_0 \gtrsim 100$, the growth parameter defined by Eq. (21) oscillates around the expected value when it is calculated from $h_{u,99}$.

Figure 3 plots the evolution of Reynolds stress maxima as a function of time. Again, from previous experimental observation [56], it is expected that the normalized turbulence kinetic energy (TKE) $k = \frac{1}{2}R_{ii}$ should approach a steady-state maximum of around 0.035. Figure 3 indicates that during the early transition process, $k/(\Delta U)^2$ peaks at a value around 0.048 before decreasing to a steady-state value around 0.03
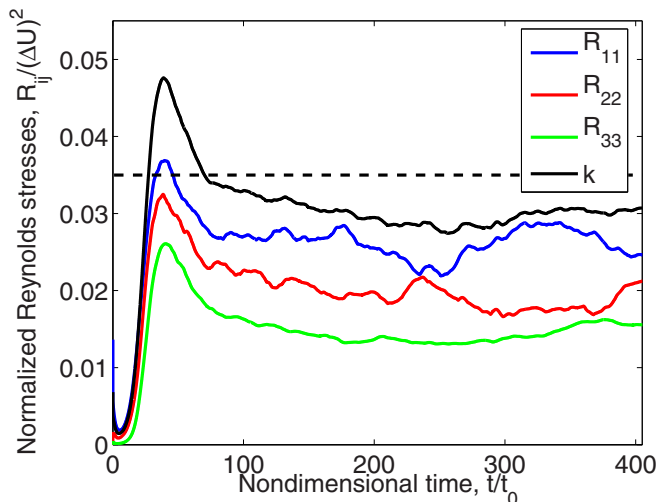
for $t/t_0 \gtrsim 100$, about 14% lower than expected. Limited variation in Re_Δ suggests that the steady-state value could be sensitive to Reynolds number and that pushing towards higher Re_Δ would likely see the computational result approach the expected experimental value.

From Figs. 2 and 3 it seems that the mixing layer transitions to turbulence approximately during the time $t/t_0 = 0$–100 and then achieves reasonably steady growth for $t/t_0 \gtrsim 100$. As Fig. 4 indicates, by $t/t_0 = 400$ both the scalar and velocity spectra have achieved inertial ranges conforming to a $-\frac{5}{3}$ scaling that span between one and two decades. The spectra in Fig. 4 are computed from 2D Fourier transforms at the nominal center plane of the mixing layer at $z = 0$. It is interesting to note that the scalar field seems to demonstrate a more fully developed inertial range than the velocity field at $\text{Re}_\Delta = 100$. Limited variation in Reynolds number has indicated that the two spectra appear to collapse by $\text{Re}_\Delta = 500$. It is also clear from Fig. 4 that the low-wave-number end of the spectra is saturated, which could suggest

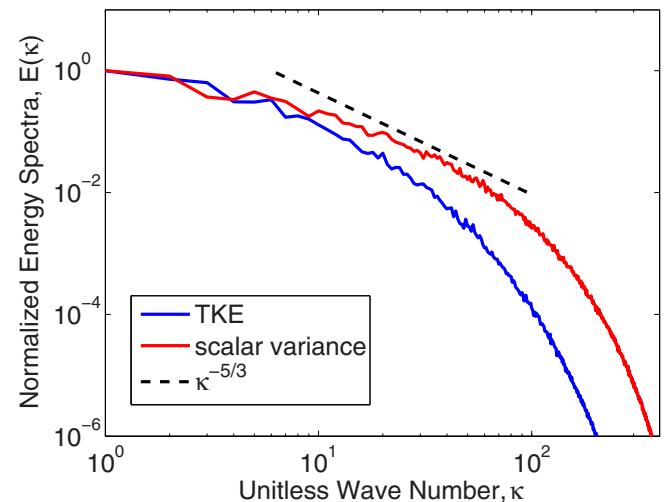FIG. 3. Evolution of Reynolds stress maxima as a function of time.

FIG. 4. Energy spectral density of the velocity and scalar fields at $t/t_0 = 400$, arbitrarily normalized by the magnitude at $\kappa = 1$.
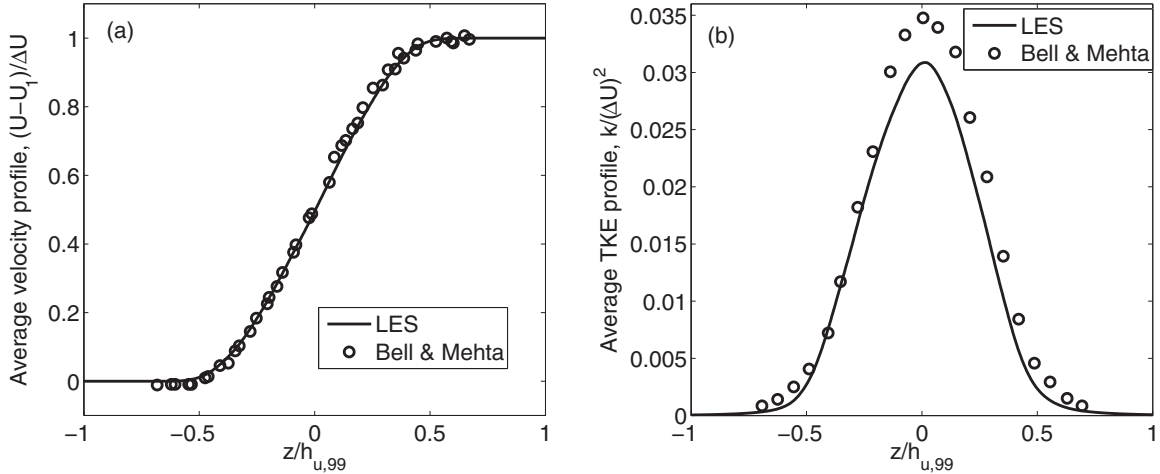
FIG. 5. Comparison of two average profiles with experimental data by Bell and Mehta [56]: (a) average streamwise velocity profile and (b) average TKE profile.

a late-time impact due to the finite size of the simulation domain.

Figures 5–7 compare LES profiles averaged over $t/t_0 = 100$–400 with experimental data from Bell and Mehta [56]. Beginning with Fig. 5, it is clear that during this time frame, the average streamwise velocity profile matches quite closely with experiment; although the peak $k/(\Delta U)^2$ in the simulation appears slightly lower than experiment, this is consistent with earlier observations in Fig. 3. Figure 6(a) additionally compares the streamwise (R_{11}) Reynolds stress, stream-normal Reynolds stress (R_{33}), and primary shear stress (R_{13}) profiles with Bell and Mehta [56]. These profiles again show reasonably good agreement with the experiment; however, it is observed that the average R_{11} and R_{22} magnitudes are somewhat underpredicted. Figure 6(b) further compares the shear correlation coefficient C_{13} defined by

$$C_{13} \equiv \frac{-\widetilde{u''w''}}{(\widetilde{u''u''})^{1/2}(\widetilde{w''w''})^{1/2}}, \tag{22}$$

where u indicates the streamwise component of velocity and w indicates the stream-normal component of velocity. A slight overprediction in the shear correlation coefficient indicates that, although the magnitude of the streamwise Reynolds stress in the LES is somewhat low compared with experiment, the relative proportion of shear to normal stress is approximately maintained. Finally, in Fig. 7, the triple correlation $\widetilde{u''w''w''}$, which represents the primary correlation associated with shear stress transport, is compared with experiment. Although the qualitative behavior of this term is maintained, the LES underpredicts peak magnitude by about 30%. Overall, however, Figs. 5–7 seem to indicate a generally good level of agreement with experiment and serve to build confidence in the accuracy of the LES.

Having established that the LES solution reaches a steady-state growth and that velocity statistics agree reasonably well with experiment, we next consider the mixing statistics of a passive scalar. Figure 8(a) plots the scalar mixedness as a function of time; recall that mixedness was defined earlier in Eq. (1). Interestingly, the mixedness follows a temporal
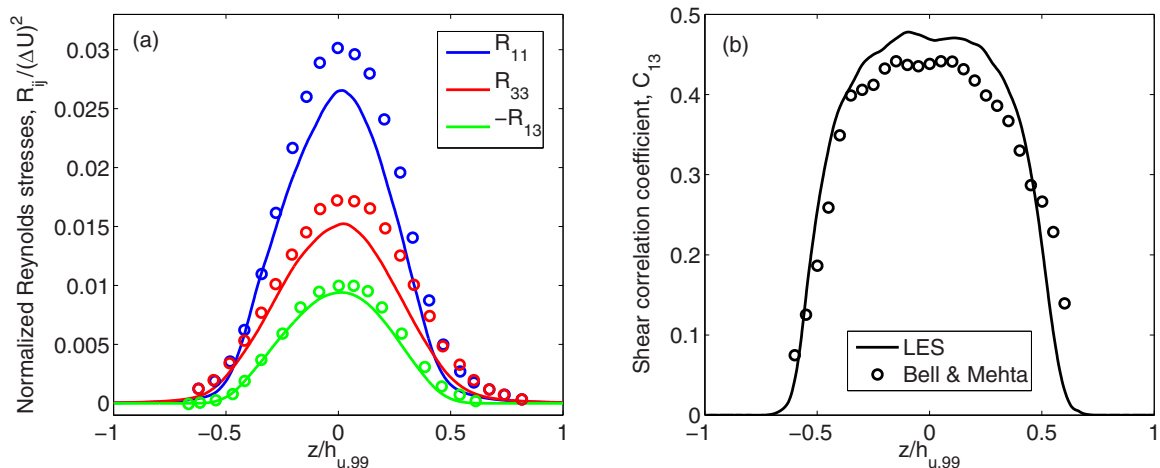

FIG. 6. Comparison of average Reynolds stress profiles with experimental data by Bell and Mehta [56]: (a) Reynolds stress profiles and (b) shear correlation coefficient, C_{13}. Symbols (○) indicate experimental data and solid lines indicate present LES.
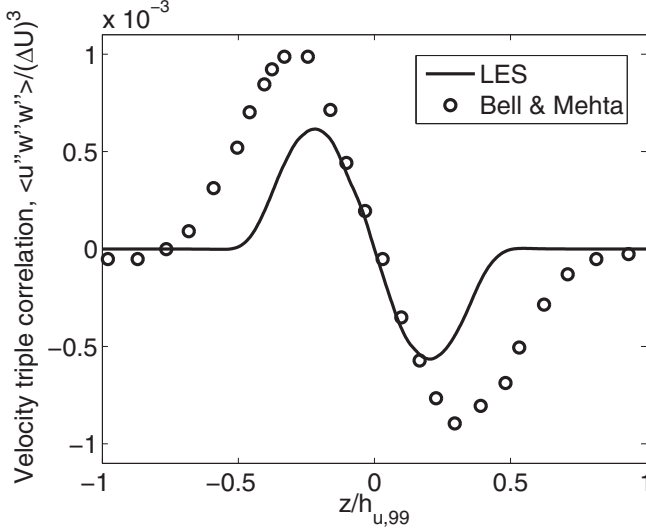
FIG. 7. Comparison of the primary shear stress transport correlation $\widetilde{u''w''w''}/(\Delta U)^3$ with experimental data by Bell and Mehta [56].

evolution that is fairly similar to what has been observed previously for RT instability [71–73]. At early time, the mixedness drops low as pretransitional mixing is dominated by large-scale entrainment. After the mixing layer transitions to turbulence, the mixedness approaches a steady-state value around $\Theta \approx 0.8$. Three time instances are indicated in Fig. 8 by colored symbols. These times correspond to times at which instantaneous profiles are considered in subsequent plots. For instance, in Fig. 8(b), spatial profiles of the scalar variance $\widetilde{Y''Y''}$ are plotted at three time instants and for the average $t/t_0 = 100$–400. The magnitude and shape of the average generally agree with similar profiles reported by Pantano *et al.* [67]. Additionally, we see that as the mixedness oscillates over time, so too does the magnitude of the scalar variance profile.

Figures 9 and 10 plot spatial profiles of scalar fluxes and scalar variance fluxes in the stream-normal and streamwise directions at the three time instants indicated in Fig. 8(a) and for the time average $t/t_0 = 100$–400. The stream-normal scalar flux in Fig. 9(a) is observed to take on a fairly smooth Gaussian-like profile similar to the Reynolds stress profiles, while the streamwise scalar flux in Fig. 10(a) demonstrates somewhat more variation across time instants. Conversely, the stream-normal scalar variance flux in Fig. 9(b) exhibits generally antisymmetric behavior about $z = 0$ similar to the shear stress transport correlation illustrated in Fig. 7. The streamwise scalar variance flux in Fig. 10(b) exhibits similar behavior, although again with more variation across time instants. In particular, at time instant $t/t_0 = 100$, there seems to be complex behavior around $z = 0$. This complex behavior at early time suggests it could be difficult to model with a simple gradient diffusion approximation.

III. RANS SIMULATION OF A KH MIXING LAYER

A. The k-2L-a-V model

The k-$2L$-a-V model represents the two-length-scale extension of the k-L-a-V model [42,43]. The model equa-

tions are derived from the compressible RANS equations for a multicomponent gas mixture. The Reynolds stress tensor, turbulence kinetic energy, mass-flux velocity vector, and density-specific-volume covariance are defined, respectively, by

$$\overline{\rho} R_{ij} \equiv \overline{\rho u_i'' u_j''}, \tag{23a}$$

$$\overline{\rho} k \equiv \tfrac{1}{2} \overline{\rho u_i'' u_i''}, \tag{23b}$$

$$a_i \equiv -\overline{u_i''}, \tag{23c}$$

$$b \equiv -\overline{\rho' \left(\frac{1}{\rho}\right)'}. \tag{23d}$$

Equations (24)–(37) below summarize the k-$2L$-a-V model, where $\widetilde{Y}_k$ is the mass fraction of specie k, μ_t is the eddy viscosity, g_j is the gravitational acceleration vector, e is the specific internal energy, L_t is the turbulent transport length scale, L_d is the turbulent destruction length scale, and V_α is the model variable for variance of the mass fraction of species α. The model coefficients C_μ, C_a, C_b, C_B, C_D, C_{L1}, C_{L2t}, C_{L2d}, C_{L3t}, C_{L3d}, C_{V1}, C_{V2}, C_{V3}, N_a, N_e, N_k, N_{Lt}, N_{Ld}, N_V, N_Y, and C_{dev} are determined through similarity analysis. The model equations are

$$\frac{D\overline{\rho}}{Dt} = -\overline{\rho} \frac{\partial \widetilde{u}_i}{\partial x_i}, \tag{24}$$

$$\overline{\rho} \frac{D\widetilde{Y}_k}{Dt} = \frac{\partial}{\partial x_i} \left(\frac{\mu_t}{N_Y} \frac{\partial \widetilde{Y}_k}{\partial x_i} \right), \tag{25}$$

$$\overline{\rho} \frac{D\widetilde{u}_j}{Dt} = \overline{\rho} g_j - \frac{\partial \overline{p}}{\partial x_j} - \frac{\partial}{\partial x_i} (\overline{\rho} R_{ij}), \tag{26}$$

$$\overline{\rho} \frac{D\widetilde{e}}{Dt} = -\overline{p} \frac{\partial \widetilde{u}_i}{\partial x_i} - a_i \frac{\partial \overline{p}}{\partial x_i} + C_D \frac{\overline{\rho}(2k)^{3/2}}{L_d} + \frac{\partial}{\partial x_i} \left(\frac{\mu_t}{N_e} \frac{\partial \widetilde{e}}{\partial x_i} \right), \tag{27}$$

$$\overline{\rho} \frac{Dk}{Dt} = -\overline{\rho} R_{ij} \frac{\partial \widetilde{u}_i}{\partial x_j} + a_i \frac{\partial \overline{p}}{\partial x_i} - C_D \frac{\overline{\rho}(2k)^{3/2}}{L_d} + \frac{\partial}{\partial x_i} \left(\frac{\mu_t}{N_k} \frac{\partial k}{\partial x_i} \right), \tag{28}$$

$$\overline{\rho} \frac{DL_t}{Dt} = C_{L1} \overline{\rho} \sqrt{2k} + C_{L2t} \overline{\rho} L_t \frac{\partial \widetilde{u}_i}{\partial x_i} - C_{L3t} \overline{\rho} R_{ij} \frac{L_t}{k} \frac{\partial \widetilde{u}_i}{\partial x_j}$$
$$+ \frac{\partial}{\partial x_i} \left(\frac{\mu_t}{N_{Lt}} \frac{\partial L_t}{\partial x_i} \right), \tag{29}$$

$$\overline{\rho} \frac{DL_d}{Dt} = C_{L1} \overline{\rho} \sqrt{2k} + C_{L2d} \overline{\rho} L_d \frac{\partial \widetilde{u}_i}{\partial x_i} - C_{L3d} \overline{\rho} R_{ij} \frac{L_d}{k} \frac{\partial \widetilde{u}_i}{\partial x_j}$$
$$+ \frac{\partial}{\partial x_i} \left(\frac{\mu_t}{N_{Ld}} \frac{\partial L_d}{\partial x_i} \right), \tag{30}$$

$$\overline{\rho} \frac{Da_j}{Dt} = C_B^2 C_b b \frac{\partial \overline{p}}{\partial x_j} - C_a \overline{\rho} a_j \frac{\sqrt{2k}}{L_d} - R_{ij} \frac{\partial \overline{\rho}}{\partial x_i}$$
$$+ \frac{\partial}{\partial x_i} \left(\frac{\mu_t}{N_a} \frac{\partial a_j}{\partial x_i} \right), \tag{31}$$

$$\overline{\rho} \frac{DV_\alpha}{Dt} = C_{V1} \mu_t \frac{\partial \widetilde{Y}_k}{\partial x_i} \frac{\partial \widetilde{Y}_k}{\partial x_i} - C_{V2} \overline{\rho} \frac{\sqrt{2k}}{L_d} V_\alpha - C_{V3} a_i \frac{V_\alpha}{b} \frac{\partial \overline{\rho}}{\partial x_i}$$
$$+ \frac{\partial}{\partial x_i} \left(\frac{\mu_t}{N_V} \frac{\partial V_\alpha}{\partial x_i} \right), \tag{32}$$
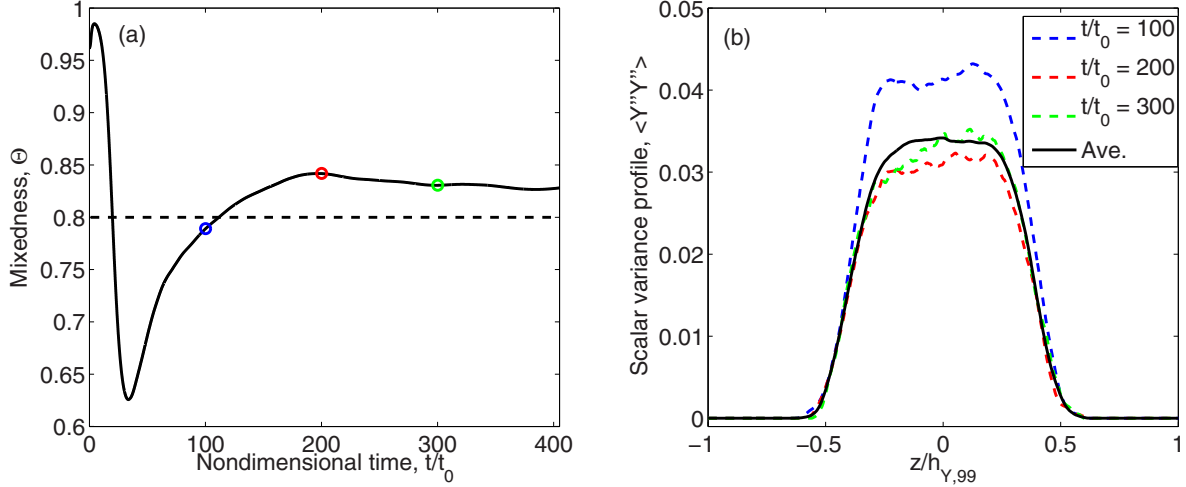
FIG. 8. Evolution of the scalar variance: (a) mixedness as a function of time and (b) spatial profiles of the scalar variance $\widetilde{Y''Y''}$ at three time instants and for the average $t/t_0 = 100$–400.

where

$$\frac{D}{Dt} \equiv \frac{\partial}{\partial t} + \widetilde{u}_i \frac{\partial}{\partial x_i}, \tag{33}$$

$$\mu_t = C_\mu \overline{\rho} \sqrt{2k} L_t, \tag{34}$$

$$\widetilde{S}_{ij} = \frac{1}{2}\left(\frac{\partial \widetilde{u}_i}{\partial x_j} + \frac{\partial \widetilde{u}_j}{\partial x_i}\right) - \frac{1}{3}\frac{\partial \widetilde{u}_k}{\partial x_k}\delta_{ij}, \tag{35}$$

$$\overline{\rho}R_{ij} = -C_{\mathrm{dev}}2\mu_t \widetilde{S}_{ij} + \frac{2}{3}\overline{\rho}k\delta_{ij}. \tag{36}$$

For the special case of binary mixing, $V_1 = V_2 = V$, and Ristorcelli [78] derived the following expression, which is utilized here to close b:

$$b = \left(\frac{r\overline{\rho}}{\rho_H}\right)^2 V. \tag{37}$$

In Eq. (37), r is a constant factor that can be written in terms of the Atwood number $A \equiv \frac{\rho_H - \rho_L}{\rho_H + \rho_L}$ or as a ratio of the heavy

fluid density ρ_H to the light fluid density ρ_L,

$$r \equiv \frac{\rho_H}{\rho_L} - 1 = \frac{2A}{1 - A}. \tag{38}$$

The model equations above differ from previously published versions of the model [42–44] primarily by the inclusion of an additional buoyancy production term on the right-hand side of Eq. (32) (i.e., the term involving C_{V3}). This term is inspired by enthalpic production mechanisms included in similar models that solve a transport equation for density variance [29,32]. The particular form that appears in Eq. (32) comes from analogy to the transport equation for b written by Besnard *et al.* [31]. In the work by Besnard *et al.* and in subsequent development of the so-called BHR model [31,35,36,39], a production term of the form $(\frac{b+1}{\overline{\rho}})a_i \frac{\partial \overline{\rho}}{\partial x_i}$ appears in the model equation for b. This term derives from transformation of a dilatational production term in the governing equation for the average specific volume [31]. As shown
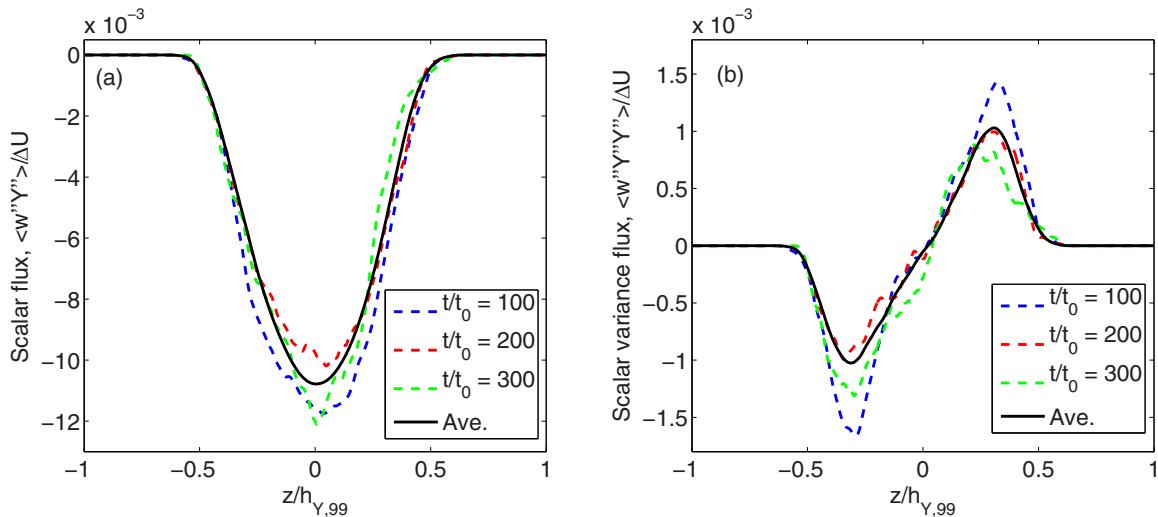

FIG. 9. Normalized spatial profiles of scalar fluxes in the stream-normal direction at three time instants and for the average $t/t_0 = 100$–400: (a) scalar flux $\widetilde{w''Y''}/\Delta U$ and (b) scalar variance flux $\widetilde{w''Y''Y''}/\Delta U$.
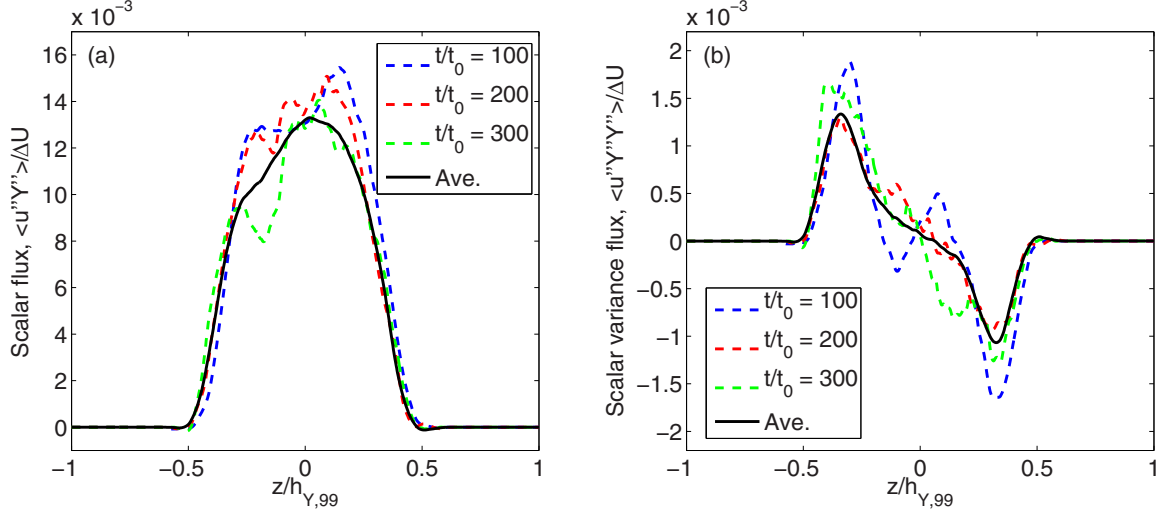
FIG. 10. Normalized spatial profiles of scalar fluxes in the streamwise direction at three time instants and for the average $t/t_0 = 100\text{–}400$: (a) scalar flux $\widetilde{u''Y''}/\Delta U$ and (b) scalar variance flux $\widetilde{u''Y''Y''}/\Delta U$.

by Ristorcelli [78], b and V are expected to be related by Eq. (37). Thus, an additional production term of the form $a_i \frac{\partial \overline{\rho}}{\partial x_i}$ is here postulated for inclusion in the model equation governing transport of V as well. From prior similarity analyses it has been shown that the self-similar magnitudes of a_i and b assume a dependence on Atwood number [38,43]. Thus, to remove the self-similar Atwood-number dependence while maintaining correct dimensionality and expected self-similar profile, the buoyancy production term used in the present work is multiplied by the ratio $\frac{V}{b}$, which results in the form used in Eq. (32). As Sec. III B will discuss next, both production terms are necessary to simultaneously match steady-state mixedness of an RT mixing layer and steady-state mixedness of a KH mixing layer.

B. Similarity analysis

Previous work [38,42,43] has shown that a set of model coefficients can be derived for the k-$2L$-a-V model which satisfy an ansatz of self-similar growth for canonical RT, RM, and KH flows. When self-similarity constraints are satisfied, the k-$2L$-a-V model has been previously shown to reproduce experimentally observable parameters, such as RT and KH growth rates, as well as the mixedness of an RT mixing layer.

1. Similarity analysis for a quasi-1D KH mixing layer

We now build on the previous work by considering the mixedness of a KH mixing layer. To begin, we assume a constant density, and a change of variable is introduced in terms of the mixing layer half-width $h(t)$. Let $\chi \equiv x/h$. It is assumed that k, L_t, L_d, and V are separable in space and time such that $k(\chi, t) = K_0(t) f(\chi)$, $L_t(\chi, t) = L_{t0}(t)\sqrt{f(\chi)}$, $L_d(\chi, t) = L_{d0}(t)\sqrt{f(\chi)}$, and $V(\chi, t) = V_0(t) f(\chi)$ with $f(\chi) = 1 - \chi^2$. A linear scalar profile is assumed such that

$$\widetilde{Y}(\chi) = \tfrac{1}{2}(1 - \chi). \tag{39}$$

Substituting Eq. (39) into Eq. (1) allows us to derive the following simple expression for the mixedness of a KH layer:

$$\Theta_{\mathrm{KH}} = 1 - 4V_0. \tag{40}$$

In Sec. II C, Θ_{KH} was determined to approach a value of about 0.8 for a fully developed mixing layer. For a quasi-1D KH mixing layer, the buoyancy production term drops out of Eq. (32), reducing it to

$$\overline{\rho}\frac{DV}{Dt} = C_{V1}\mu_t\left(\frac{\partial \widetilde{Y}}{\partial x}\right)^2 - C_{V2}\overline{\rho}\frac{\sqrt{2k}}{L_d}V + \frac{\partial}{\partial x}\left(\frac{\mu_t}{N_V}\frac{\partial V}{\partial x}\right). \tag{41}$$

Substituting into Eq. (41) and assuming incompressibility leads to

$$\frac{D}{Dt}(V_0 f) = C_{V1}C_\mu L_{t0}\sqrt{2K_0}\left(-\frac{1}{2h}\right)^2 f$$
$$- C_{V2}\frac{\sqrt{2K_0}}{L_{d0}}V_0 f + \frac{\partial}{\partial x}\left[\frac{C_\mu L_{t0} f \sqrt{2K_0}}{N_V}\frac{\partial}{\partial x}(V_0 f)\right]. \tag{42}$$

According to the similarity ansatz, the turbulence length scale is assumed to grow self-similarly such that $L_{t0} = \beta h$. From prior self-similarity analysis of the two-length-scale model applied to a KH mixing layer [42], the following expressions have been previously determined:

$$\beta^2 = \frac{4C_{L1}N_{Lt}}{8C_\mu - C_\mu N_{Lt}C_{L3t}C_{\mathrm{dev}}\Phi} \tag{43}$$

and

$$\dot{L}_{t0} = \frac{4C_{L1}}{8 - N_{Lt}C_{L3t}C_{\mathrm{dev}}\Phi}\sqrt{2K_0}. \tag{44}$$

In Eqs. (43) and (44), the variable $\Phi \equiv \frac{(\Delta U)^2}{k}$ is the inverse of the turbulence intensity. In addition, prior analysis [42] has determined the following relationship for the steady-state ratio of length scales:

$$\frac{L_{d0}}{L_{t0}} = \left(\frac{N_{Ld}}{N_{Lt}}\right)\left(\frac{8 - N_{Lt}C_{L3t}C_{\mathrm{dev}}\Phi}{8 - N_{Ld}C_{L3d}C_{\mathrm{dev}}\Phi}\right). \tag{45}$$

Recognizing from Eq. (40) that $\dot{V}_0 = 0$ in the self-similar regime, after some algebra and substitution of Eqs. (43)–(45), Eq. (42) can be rearranged to give

$$
\left[8C_{L1}V_0 + C_{V1}C_{L1}N_{Lt} - C_{V2}V_0\left(\frac{N_{Lt}}{N_{Ld}}\right)(8 - N_{Ld}C_{L3d}C_{\text{dev}}\Phi) - 24C_{L1}\frac{N_{Lt}}{N_V}V_0 \right]\chi^2
$$
$$
- \left[C_{V1}C_{L1}N_{Lt} - C_{V2}V_0\left(\frac{N_{Lt}}{N_{Ld}}\right)(8 - N_{Ld}C_{L3d}C_{\text{dev}}\Phi) - 8C_{L1}\frac{N_{Lt}}{N_V}V_0 \right] = 0. \tag{46}
$$

To ensure that both the χ^2 terms and the constant terms in Eq. (46) go to zero simultaneously requires

$$
N_V = 2N_{Lt}. \tag{47}
$$

Substituting Eq. (47) back into Eq. (46) reduces both sets of terms in square brackets to

$$
C_{V1}C_{L1}N_{Lt} - 4C_{L1}V_0
$$
$$
- C_{V2}V_0\left(\frac{N_{Lt}}{N_{Ld}}\right)(8 - N_{Ld}C_{L3d}C_{\text{dev}}\Phi) = 0, \tag{48}
$$

which can be rearranged to solve for the following constraint on C_{V1} in terms of Θ_{KH}:

$$
C_{V1} = \left[\frac{8C_{V2}}{C_{L1}N_{Ld}} - C_{V2}C_{\text{dev}}\Phi\frac{C_{L3d}}{C_{L1}} + \frac{4}{N_{Lt}} \right]\left(\frac{1 - \Theta_{\text{KH}}}{4}\right). \tag{49}
$$

Alternatively, Eq. (49) can be rearranged to solve for Θ_{KH},

$$
\Theta_{\text{KH}} = 1 - \frac{4C_{V1}N_{Lt}}{8\frac{C_{V2}}{C_{L1}} - C_{V2}C_{\text{dev}}N_{Lt}\Phi\frac{C_{L3d}}{C_{L1}} + 4}, \tag{50}
$$

where the result that $N_{Lt} = N_{Ld}$ [42] has been used to simplify Eq. (49).

2. Similarity analysis for a 1D RT mixing layer

Next the model equations are considered for a 1D RT mixing layer in the limit of zero Atwood number. In this case, the buoyancy production term in Eq. (32) is retained,

$$
\rho\frac{DV}{Dt} = C_{V1}\mu_t\left(\frac{\partial Y}{\partial x}\right)^2 - C_{V2}\rho\frac{\sqrt{2k}}{L_d}V
$$
$$
- C_{V3}a\frac{V}{b}\frac{\partial\overline{\rho}}{\partial x_i} + \frac{\partial}{\partial x}\left(\frac{\mu_t}{N_V}\frac{\partial V}{\partial x}\right). \tag{51}
$$

As before, the RT mixedness is determined by substituting into Eq. (1),

$$
\Theta_{\text{RT}} = 1 - 4V_0. \tag{52}
$$

Again referring to earlier published similarity analysis [38,43], the self-similar profiles of the mass-flux velocity a and the density-specific-volume covariance b are, respectively,

$$
a = -C_B\frac{A}{1 - A^2}\sqrt{2K_0}f \tag{53}
$$

and

$$
b = \frac{4A^2}{1 - 2A^2 + A^4}V_0 f, \tag{54}
$$

where A is the conventional Atwood number. Substituting back into Eq. (51) and applying the low-Atwood-number approximation leads to

$$
\frac{D}{Dt}(V_0 f)
$$
$$
= C_{V1}C_\mu L_{t0}\sqrt{2K_0}\left(-\frac{1}{2h}\right)^2 f - C_{V2}\frac{\sqrt{2K_0}}{L_{d0}}V_0 f
$$
$$
+ C_{V3}C_B\sqrt{2K_0}\left(\frac{1}{h}\right)f + \frac{\partial}{\partial x}\left[\frac{C_\mu L_{t0}f\sqrt{2K_0}}{N_V}\frac{\partial}{\partial x}(V_0 f)\right]. \tag{55}
$$

For an RT mixing layer, the relationship between L_{t0} and h is somewhat simpler than in the case of a KH mixing layer [38] such that

$$
\beta^2 = \frac{C_{L1}N_{Lt}}{2C_\mu} \tag{56}
$$

and

$$
\dot{L}_{t0} = \frac{C_{L1}}{2}\sqrt{2K_0}. \tag{57}
$$

Then, substituting back into Eq. (55) and recognizing for an RT layer that $L_{t0} = L_{d0}$, the following expression is obtained:

$$
\left[C_{L1t}V_0 + \frac{C_{V1}C_{L1t}N_{Lt}}{8} - C_{V2}V_0 + \frac{C_{V3}C_B}{4}\sqrt{\frac{C_{L1}N_{Lt}}{2C_\mu}} \right.
$$
$$
\left. - \frac{3C_{L1}N_{Lt}}{N_V}V_0 \right]\chi^2 - \left[\frac{C_{V1}C_{L1t}N_{Lt}}{8} - C_{V2}V_0 \right.
$$
$$
\left. + \frac{C_{V3}C_B}{4}\sqrt{\frac{C_{L1}N_{Lt}}{2C_\mu}} - \frac{C_{L1}N_{Lt}}{N_V}V_0 \right] = 0. \tag{58}
$$

Again, it is required that $N_V = 2N_{Lt}$ in order to simultaneously solve both sets of bracketed terms. Utilizing this constraint reduces both sets of terms in Eq. (58) to the expression

$$
\frac{C_{V1}C_{L1}N_{Lt}}{8} + \frac{C_{V3}C_B}{4}\sqrt{\frac{C_{L1}N_{Lt}}{2C_\mu}}
$$
$$
- \left(C_{V2} + \frac{C_{L1}}{2}\right)\left(\frac{1 - \Theta_{\text{RT}}}{4}\right) = 0. \tag{59}
$$

Then rearranging Eq. (59) to solve for C_{V3} gives the constraint

$$
C_{V3} = \frac{(2C_{V2} + C_{L1})(1 - \Theta_{\text{RT}}) - C_{V1}C_{L1}N_{Lt}}{2C_B}\sqrt{\frac{2C_\mu}{C_{L1}N_{Lt}}}. \tag{60}
$$

TABLE I. Summary of the k-$2L$-a-V model coefficients. Differences are indicated with bold text.

Θ_{RT}	Θ_{KH}	C_μ	C_{dev}	C_a	C_b	C_B	C_D	C_{L1}	C_{L2t}	C_{L2d}	C_{L3t}	C_{L3d}	C_{V1}	C_{V2}	C_{V3}	$N_{Lt,Ld}$	$N_{a,e,k,V,Y}$
0.800	**0.657**	1.00	0.404	1.46	5.00	0.553	1.24	0.990	-5.83	0.515	-9.24	0.272	**1.131**	2.97	**0.000**	1.24	2.48
0.800	**0.800**	1.00	0.404	1.46	5.00	0.553	1.24	0.990	-5.83	0.515	-9.24	0.272	**0.660**	2.97	**0.666**	1.24	2.48

Alternatively, Eq. (60) can be rearranged to solve for Θ_{RT},

$$\Theta_{RT} = 1 - \frac{2C_B C_{V3}\sqrt{\frac{C_{L1}N_{Lt}}{2C_\mu}} + C_{V1}C_{L1}N_{Lt}}{2C_{V2} + C_{L1}}. \quad (61)$$

Now utilizing Eqs. (49) and (60), it is possible to derive a set of model coefficients in terms of the desired self-similar mixedness of both an RT and a KH mixing layer. Table I summarizes the complete set of model coefficients, where the remainder of model coefficients are determined by constraints previously derived [38,42–44] to enforce an RT growth parameter $\alpha_b = 0.025$, an RT energy ratio of 0.5, a KH turbulence intensity of $\Phi^{-1} = 0.035$, a KH growth parameter of $\delta/\mathcal{A} = 0.08$, an homogeneous isotropic turbulence (HIT) TKE decay exponent $n = 1.11$, and an HIT scalar decay exponent $m = 1.33$. Two sets of model coefficients are given in Table I, which illustrate that for a model that does not include the buoyancy production term in Eq. (32) (i.e., a model in which $C_{V3} = 0$), the expected mixedness for a KH mixing layer is 0.657, a value which is significantly lower than expected based on the LES calculations discussed previously in Sec. II C. On the other hand, if the buoyancy production term is included and the values of C_{V1} and C_{V3} are computed according to Eqs. (49) and (60), then both the self-similar mixedness of an RT mixing layer and the self-similar mixedness of a KH mixing layer can be set to 0.8.

C. Problem setup and initial conditions

Reynolds-averaged Navier-Stokes simulations with the k-$2L$-a-V model are computed with the ARES code, which is a second-order arbitrary Lagrangian-Eulerian hydrodynamics code developed at Lawrence Livermore National Laboratory

[40,43]. In the next section, simulations are performed of both a 1D RT mixing layer and a quasi-1D KH mixing layer.

For RT mixing layer simulations, two ideal monatomic gases are considered subject to constant acceleration at $A = 0.05$. This problem is set up in a domain of size of 1 cm with 1600 uniformly spaced computational zones. Turbulence length scales are initialized to zero everywhere except for the two zones bordering the interface at $z = 0$, where $L_d = L_t = 4.0 \times 10^{-6}$ cm. Turbulence kinetic energy is initialized to zero everywhere except the two interface zones, where k is initialized to 1.0 cm^2/s^2.

Kelvin-Helmholtz mixing layer simulations are run with 960 uniformly spaced computational zones on a domain extending from $z = -48.0$ cm to $z = 48.0$ cm. Turbulence length scales are initialized to zero everywhere except for the two zones bordering the interface at $z = 0$, where $L_d = L_t = 0.44$ cm. Turbulence kinetic energy is additionally initialized to zero everywhere except for the two interface zones, where k is initialized to $0.01(\Delta U)^2$. The initial velocity profile is chosen to match the Bell and Mehta experiment [56] and the LES results in Sec. II C such that $u = U_1 = 900$ cm/s for $z < 0$ and $u = U_2 = 1500$ cm/s for $z \geqslant 0$, corresponding to $\mathcal{A} = 0.25$.

D. Results and discussion

To examine the impact of the buoyancy production term in Eq. (32), two simulations of the KH mixing layer described in Sec. III C are conducted using the two sets of model coefficients summarized in Table I. Figures 11 and 12 compare basic metrics of mixing layer growth rate and turbulence intensity between the two simulations. Of course, since the
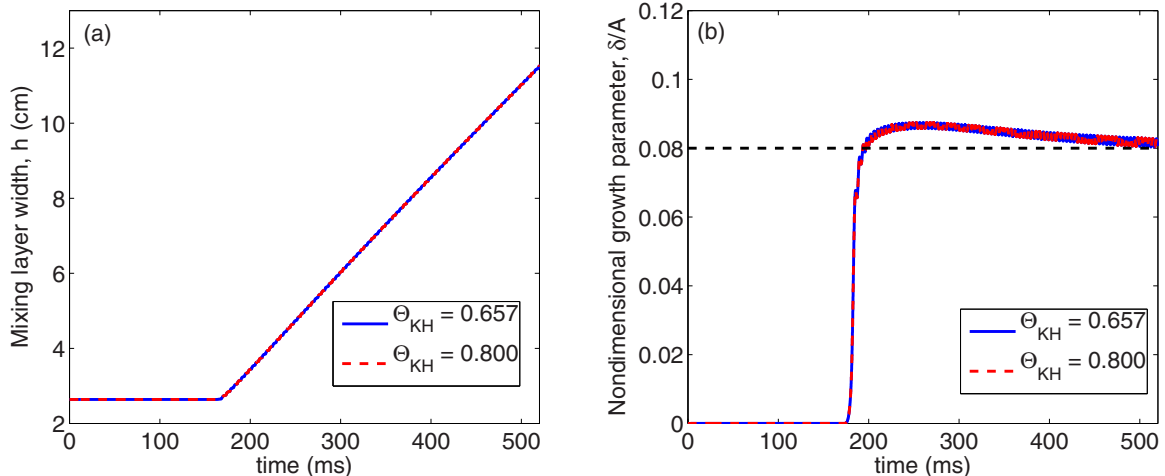

FIG. 11. Mixing layer growth for RANS simulations of a KH mixing layer with two different sets of model coefficients: (a) mixing layer width as a function of time and (b) KH growth parameter $\delta/\mathcal{A}$ as a function of time.
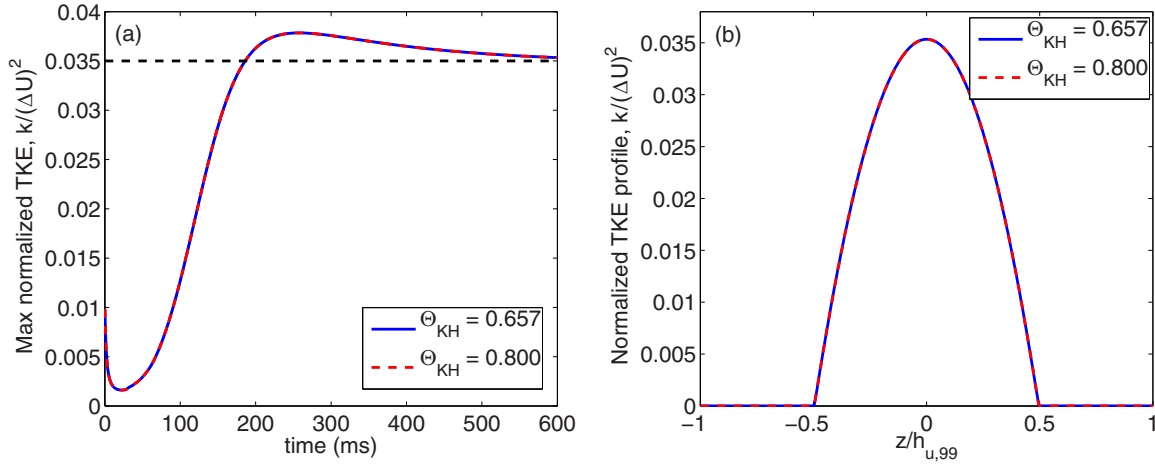
FIG. 12. TKE in RANS simulations of a KH mixing layer with two different sets of model coefficients: (a) maximum normalized TKE $k/(\Delta U)^2$ as a function of time and (b) steady-state TKE profile across the mixing layer at the simulation end time.

buoyancy production term in Eq. (32) is zero for KH mixing, the two simulations are not expected to be different in these metrics, and in fact no difference is observed in Figs. 11 and 12. Figure 11 does illustrate that both simulations approach a steady-state growth parameter of $\delta/\mathcal{A} = 0.08$ as expected. Additionally, Fig. 12 illustrates that the two simulations approach a steady-state turbulence intensity $\Phi^{-1} = 0.035$ as expected. Thus, the change to model coefficients has not impacted model behavior previously obtained for KH mixing layer development [42].

Figure 13 illustrates the primary difference between the two sets of model coefficients in Table I. In this figure, the steady-state mixedness is plotted for 1D RANS simulations of an RT mixing layer [in Fig. 13(a)] and a KH mixing layer [in Fig. 13(b)] with both sets of model coefficients. As this figure illustrates, the steady-state mixedness of the RT mixing layer approaches 0.8 for both sets of model coefficients. In the KH simulations, the steady-state mixedness approaches 0.657 for the simulation that does not include the buoyancy production term in Eq. (32), while the mixedness approaches the expected

0.8 for the simulation that includes the buoyancy production term. As observed in Sec. II C, a value of $\Theta_{KH} \approx 0.8$ is more consistent with LES.

In Fig. 14, steady-state scalar variance profiles are compared among the two KH RANS simulations and from LES previously discussed in Sec. II C. Consistent with the previously remarked discrepancy in mixedness behavior, Fig. 14 illustrates that the peak magnitude of scalar variance agrees more closely with LES for the case calibrated to give $\Theta_{KH} = 0.8$. In other words, if a model with only a single scalar variance production mechanism is calibrated to reproduce the RT mixedness, it will likely overpredict scalar variance production due to shear. Equivalently, if a model with a single production mechanism is calibrated to reproduce the KH mixedness, it will likely underpredict scalar variance production in an RT mixing layer.

Profiles of scalar and scalar variance turbulent fluxes are plotted in Fig. 15. In this figure, RANS fluxes are reconstructed from the gradient diffusion closure where for a model variable f with diffusion coefficient N_f, the turbulent flux is
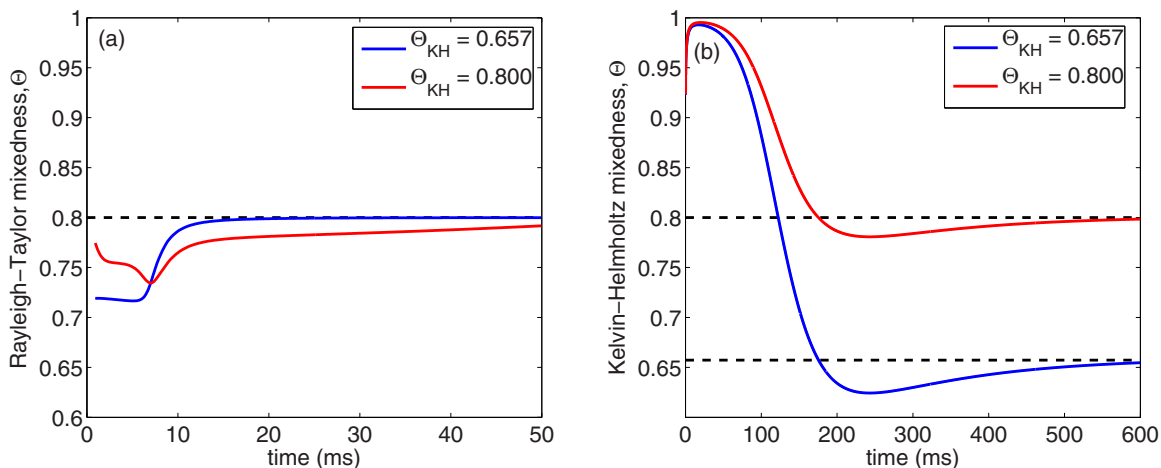

FIG. 13. Steady-state mixedness in RANS simulations using two different sets of model coefficients: (a) mixedness in an RT mixing layer and (b) mixedness in a KH mixing layer.
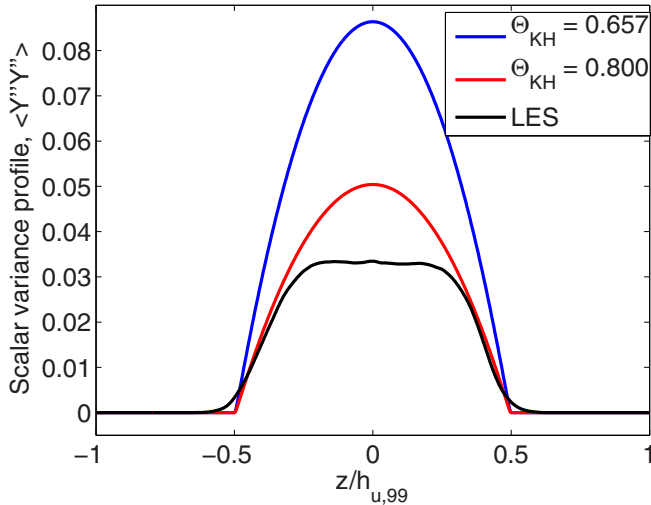
FIG. 14. Steady-state scalar variance profiles across a KH mixing layer for two different sets of RANS model coefficients.

approximated by

$$\widetilde{u_i'' f''} \approx \frac{\mu_t}{N_f} \frac{\partial f}{\partial x_i}. \tag{62}$$

While the turbulent scalar flux matches LES reasonably well with no difference between the two RANS simulations, the turbulent scalar variance flux profile demonstrates a similar difference in magnitude as was observed for the scalar variance itself in Fig. 14. While the agreement with LES is not as close as with the turbulent scalar flux, it is clear that the turbulent scalar variance flux is overpredicted in the case with $\Theta_{KH} = 0.657$, and the case with $\Theta_{KH} = 0.800$ is closer in magnitude to the LES result.

Of course, the mixing layers simulated in the present work have been nonreacting, so overprediction of the scalar variance in these simulations has not had a significant impact on metrics of interest such as growth rates and turbulence intensity. In simulations of reacting mixing layers, however, accurate prediction of the scalar variance is crucial to predicting the average reaction rate [43]. The inclusion of the buoyancy production mechanism in Eq. (32) along with the calibration procedure based on self-similarity analysis discussed in Sec. III B should therefore be considered important in simulations of reacting mixing layers, such as in ICF applications, which may involve mixing due to combined shear and buoyancy mechanisms.

IV. SUMMARY AND CONCLUSIONS

In the present work, LES has been performed of a temporally developing shear layer in which a passive scalar tracer was transported by one fluid stream. This LES was evolved until late time in order to examine the self-similar behavior in a regime that could be compared with RANS results. Large-eddy simulation results demonstrated generally good agreement with previously published experimental data by

Bell and Mehta [56] in profiles of average velocity, turbulence kinetic energy, and Reynolds stresses. These comparisons with experiment built confidence in the quality of the LES, allowing further examination of turbulent statistics of the passive scalar.

The integral measure of scalar variance known as mixedness was found to approach a value of around 0.8, similar to behavior in self-similar RT mixing. After identifying the value of this key parameter from LES, attention was then turned towards improving the k-$2L$-a-V RANS model to allow it to match self-similar mixedness for both RT and KH mixing layers with a single set of model coefficients. It was determined that the addition of a buoyancy production term in the model equation for scalar variance introduces the necessary degree of freedom to achieve such a calibration. Self-similarity analysis was then applied to derive algebraic constraints on model coefficients that, when satisfied, would reproduce the expected self-similar mixedness behavior in RANS simulations.

The improved k-$2L$-a-V model was then applied in 1D simulations of an RT mixing layer and quasi-1D simulations of the KH mixing layer simulated with LES. It was found that the improved model reproduced the expected mixedness of 0.8 for both RT and KH mixing layers, while a model without the buoyancy production term significantly overpredicted mixedness for the KH mixing layer.

In simulations of reacting turbulence, which have not been considered in the present work but which remain the primary motivation for development of the k-$2L$-a-V model, accurate prediction of the scalar variance is crucial to prediction of the average reaction rate. Reacting RT mixing layers were simulated previously by Morgan *et al.* [43], and the k-$2L$-a-V model was demonstrated to match LES data quite well. As the present work has demonstrated, however, should the earlier version of the k-$2L$-a-V model used by Morgan *et al.* [43] be applied to simulation of a reacting shear layer or a reacting mixing layer with combined elements of RT and KH instability, production of scalar variance due to shear effects, and therefore the impact of scalar variance on average reaction rate, would likely be overestimated. Fortunately, as the present work has also shown, a straightforward improvement can be made that allows for improved prediction of scalar variance production due to combined effects of buoyancy and shear.

Of course, more work remains to be done. The improved k-$2L$-a-V model should be compared against suitable high-fidelity simulation or experimental data for complex, reacting turbulent mixing with combined elements of both RT and KH instability. Most likely, such an effort will require significant additional computation and is therefore left as future work. It is expected, however, that the improved k-$2L$-a-V model discussed in the present work should perform better in such a simulation than the earlier model which has been previously applied successfully in simulation of a simpler reacting RT mixing layer [43].
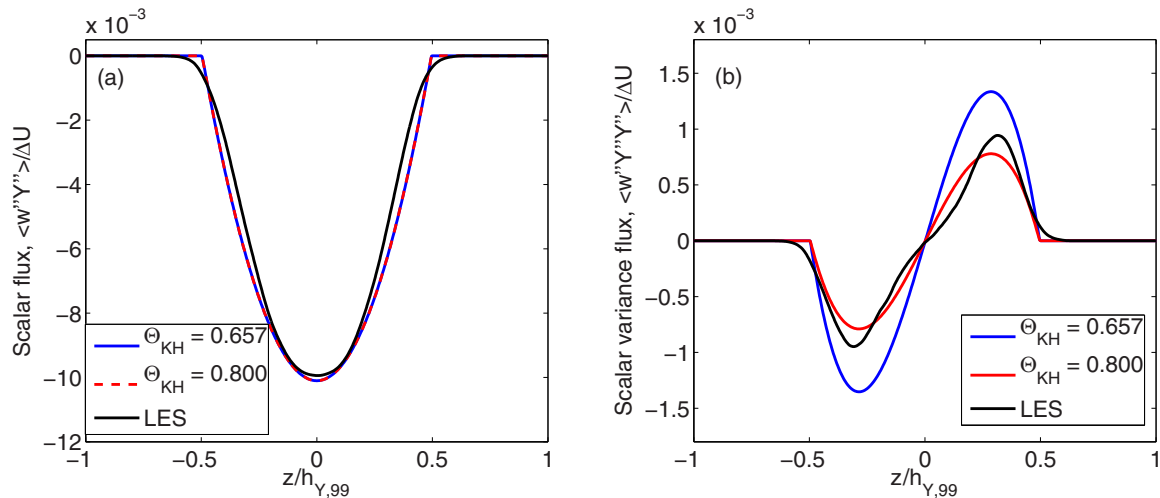
FIG. 15. Comparison with LES of steady-state turbulent flux profiles obtained from RANS simulations with two different sets of model coefficients: (a) scalar flux $\widetilde{w''Y''}/\Delta U$ and (b) scalar variance flux $\widetilde{w''Y''Y''}/\Delta U$.

[1] J. Yang, T. Kubota, and E. E. Zukoski, Applications of shock-induced mixing to supersonic combustion, AIAA J. **31**, 854 (1993).

[2] F. K. Browand and C. D. Winant, Laboratory observations of shear-layer instability in a stratified fluid, Bound.-Layer Meteorol. **5**, 67 (1973).

[3] I. P. D. De Silva, H. J. S. Fernando, F. Eaton, and D. Hebert, Evolution of Kelvin-Helmholtz billows in nature and laboratory, Earth Planet. Sci. Lett. **143**, 217 (1996).

[4] J. Werne and D. C. Fritts, Stratified shear turbulence: Evolution and statistics, Geophys. Res. Lett. **26**, 439 (1999).

[5] M. C. Kelley, C. Y. Chen, R. R. Beland, R. Woodman, J. L. Chau, and J. Werne, Persistence of a Kelvin-Helmholtz instability complex in the upper troposphere, J. Geophys. Res. **110**, D14106 (2005).

[6] D. Arnett, The role of mixing in astrophysics, Astrophys. J. Suppl. **127**, 213 (2000).

[7] J. D. Lindl, R. L. McCrory, and E. M. Campbell, Progress toward ignition and burn propagation in inertial confinement fusion, Phys. Today **45**(9), 32 (1992).

[8] J. Lindl, Development of the indirect-drive approach to inertial confinement fusion and the target physics basis for ignition and gain, Phys. Plasmas **2**, 3933 (1995).

[9] S. E. Bodner, Rayleigh-Taylor Instability and Laser-Pellet Fusion, Phys. Rev. Lett. **33**, 761 (1974).

[10] J. D. Lindl and W. C. Mead, Two-Dimensional Simulation of Fluid Instability in Laser-Fusion Pellets, Phys. Rev. Lett. **34**, 1273 (1975).

[11] W. W. Hsing, C. W. Barnes, J. B. Beck, N. M. Hoffman, D. Galmiche, A. Richard, J. Edwards, P. Graham, S. Rothman, and B. Thomas, Rayleigh-Taylor instability evolution in ablatively driven cylindrical implosions, Phys. Plasmas **4**, 1832 (1997).

[12] K. O. Mikaelian, Rayleigh-Taylor and Richtmyer-Meshkov instabilities and mixing in stratified cylindrical shells, Phys. Fluids **17**, 094105 (2005).

[13] V. A. Smalyuk, M. Barrios, J. A. Caggiano, D. T. Casey, C. J. Cerjan, D. S. Clark, M. J. Edwards, J. A. Frenje, M. Gatu-Johnson, V. Y. Glebov, G. Grim, S. W. Haan, B. A. Hammel,

A. Hamza, D. E. Hoover, W. W. Hsing, O. Hurrican, J. D. Kilkenny, J. L. Kline, J. P. Knauer *et al.*, Hydrodynamic instability growth and mix experiments at the National Ignition Facility, Phys. Plasmas **21**, 056301 (2014).

[14] V. A. Smalyuk, R. E. Tipton, J. E. Pino, D. T. Casey, G. P. Grim, B. A. Remintgon, D. P. Rowley, S. V. Weber, M. Barrios, L. R. Benedetti *et al.*, Measurements of an Ablator-Gas Atomic Mix in Indirectly Driven Implosions at the National Ignition Facility, Phys. Rev. Lett. **112**, 025002 (2014).

[15] D. T. Casey, V. A. Smalyuk, R. E. Tipton, J. E. Pino, G. P. Grim, B. A. Remington, D. P. Rowley, S. V. Weber, M. Barrios, L. R. Benedetti, D. L. Bleuel, E. J. Bond, D. K. Bradley, J. A. Caggiano, D. A. Callahan, C. J. Cerjan, K. C. Chen, D. H. Edgell, M. J. Edwards, D. Fittinghoff *et al.*, Development of the CD Symcap platform to study gas-shell mix in implosions at the National Ignition Facility, Phys. Plasmas **21**, 092705 (2014).

[16] V. A. Smalyuk, J. F. Hansen, O. A. Hurricane, G. Langstaff, D. Martinez, H.-S. Park, K. Raman, B. A. Remington, H. F. Robey, O. Schilling, R. Wallace, Y. Elbaz, A. Shimony, D. Shvarts, C. Di Stefano, R. P. Drake, D. Marion, C. M. Krauland, and C. C. Kuranz, Experimental observations of turbulent mixing due to Kelvin-Helmholtz instability on the OMEGA laser facility, Phys. Plasmas **19**, 092702 (2012).

[17] O. A. Hurricane, V. A. Smalyuk, K. Raman, O. Schilling, J. F. Hansen, G. Langstaff, D. Martinez, H.-S. Park, B. A. Remington, H. F. Robey, J. A. Greenough, R. Wallace, C. A. Di Stefano, R. P. Drake, D. Marion, C. M. Krauland, and C. C. Kuranz, Validation of a Turbulent Kelvin-Helmholtz Shear Layer Model Using and a High-Energy-Density OMEGA Laser Experiment, Phys. Rev. Lett. **109**, 155004 (2012).

[18] V. A. Smalyuk, O. A. Hurricane, J. F. Hansen, G. Langstaff, D. Martinez, H.-S. Park, K. Raman, B. A. Remington, H. F. Robey, O. Schilling, R. Wallace, Y. Elbaz, A. Shimony, D. Shvarts, C. Di Stefano, R. P. Drake, D. Marion, C. M. Krauland, and C. C. Kuranz, Measurements of turbulent mixing due to Kelvin-Helmholtz instability in high-energy-density plasmas, High Energy Density Phys. **9**, 47 (2013).

[19] F. W. Doss, J. R. Fincke, E. N. Loomis, L. Welser-Sherrill, and K. A. Flippo, The high-energy-density counterpropagating shear experiment and turbulent self-heating, Phys. Plasmas **20**, 122704 (2013).

[20] F. W. Doss, J. L. Kline, K. A. Flippo, T. S. Perry, B. G. DeVolder, I. Tregellis, E. N. Loomis, E. C. Merritt, T. J. Murphy, L. Welser-Sherrill, and J. R. Fincke, The shock/shear platform for planar radiation-hydrodynamics experiments on the National Ignition Facility, Phys. Plasmas **22**, 056303 (2015).

[21] K. A. Flippo, F. W. Doss, J. L. Kline, E. C. Merritt, D. Capelli, T. Cardenas, B. DeVolder, F. Fierro, C. M. Huntington, L. Kot, E. N. Loomis, S. A. MacLaren, T. J. Murphy, S. R. Nagel, T. S. Perry, R. B. Randolph, G. Rivera, and D. W. Schmidt, Late-Time Mixing Sensitivity to Initial Broadband Surface Roughness in High-Energy-Density Shear Layers, Phys. Rev. Lett. **117**, 225001 (2016).

[22] P. A. Bradley, J. A. Cobble, I. L. Tregillis, M. J. Schmitt, K. D. Obrey, V. Glebov, S. H. Batha, G. R. Magelssen, J. R. Fincke, S. C. Hsu, N. S. Krasheninnikova, T. J. Murphy, and F. J. Wysocki, Role of shocks and mix caused by capsule defects, Phys. Plasmas **19**, 092703 (2012).

[23] C. R. Weber, D. T. Casey, D. S. Clark, B. A. Hammel, A. MacPhee, J. Milovich, D. Martinez, H. F. Robey, V. A. Smalyuk, M. Stadermann, P. Amendt, S. Bhandarkar, B. Chang, C. Choate, J. Crippen, S. J. Felker, J. E. Field, S W. Haan, S. Johnson, J. J. Kroll *et al.*, Improving ICF implosion performance with alternative capsule supports, Phys. Plasmas **24**, 056302 (2017).

[24] A. G. MacPhee, V. A. Smalyuk, O. L. Landen, C. R. Weber, H. F. Robey, E. L. Alfonso, K. L. Baker, L. F. Berzak Hopkins, J. Biener, T. Bunn, D. T. Casey, D. S. Clark, J. W. Crippen, L. Divol, M. Farrell, S. Felker, J. E. Field, W. W. Hsing, C. Kong, S. Le Pape *et al.*, Hydrodynamic instabilities seeded by the x-ray shadow of ICF capsule fill tubes, Phys. Plasmas **25**, 082702 (2018).

[25] A. G. MacPhee, V. A. Smalyuk, O. L. Landen, C. R. Weber, H. F. Robey, E. L. Alfonso, J. Biener, T. Bunn, J. W. Crippen, M. Farrell, S. Felker, J. E. Field, W. W. Hsing, C. Kong, J. Milovich, A. Moore, A. Nikroo, N. Rice, M. Stadermann, and C. Wild, Mitigation of x-ray shadow seeding of hydrodynamic instabilities on inertial confinement fusion capsules using a reduced diameter fuel fill-tube, Phys. Plasmas **25**, 054505 (2018).

[26] C. R. Weber, D. S. Clark, A. Pak, N. Alfonso, B. Bachmann, L. F. Berzak Hopkins, T. Bunn, J. Crippen, L. Divol, T. Dittrich, A. L. Kritcher, O. L. Landen, S. Le Pape, A. G. MacPhee, E. Marley, L. P. Masse, J. L. Milovich, A. Nikroo, P. K. Patel, L. A. Pickworth *et al.*, Mixing in ICF implosions on the National Ignition Facility caused by the fill-tube, Phys. Plasmas **27**, 032703 (2020).

[27] Sir W. Thomson F.R.S. (Lord Kelvin), XLVI. Hydrokinetic solutions and observations, Philos. Mag. **42**, 362 (1871).

[28] H. Helmholtz, XLIII. On discontinuous movements of fluids, Philos. Mag. **36**, 337 (1868).

[29] D. Besnard, F. H. Harlow, and R. Rauenzahn, Conservation and transport properties of turbulence with large density variations, Technical Report No. LA-10911-MS, Los Alamos National Laboratory, US, 1987.

[30] S. Gauthier and M. Bonnet, A *k*-ε model for turbulent mixing in shock-tube flows induced by Rayleigh-Taylor instability, Phys. Fluids A **2**, 1685 (1990).

[31] D. C. Besnard, F. H. Harlow, R. M. Rauenzahn, and C. Zemach, Turbulence transport equations for variable-density turbulence and their relationship to two-field models, Technical Report No. LAUR-12303, Los Alamos National Laboratory, US, 1992.

[32] O. Grégoire, D. Souffland, and S. Gauthier, A second-order turbulence model for gaseous mixtures induced by Richtmyer-Meshkov instability, J. Turbul. **6**, 1 (2005).

[33] G. Dimonte and R. Tipton, *K-L* turbulence model for the self-similar growth of the Rayleigh-Taylor and Richtmyer-Meshkov instabilities, Phys. Fluids **18**, 085101 (2006).

[34] A. Banerjee, R. A. Gore, and M. J. Andrews, Development and validation of a turbulent-mix model for variable-density and compressible flows, Phys. Rev. E **82**, 046309 (2010).

[35] J. D. Schwarzkopf, D. Livescu, R. A. Gore, R. M. Rauenzahn, and J. R. Ristorcelli, Application of a second-moment closure model to mixing processes involving multicomponent miscible fluids, J. Turbul. **12**, N49 (2011).

[36] B. M. Haines, F. F. Grinstein, and J. D. Schwarzkopf, Reynolds-averaged Navier-Stokes initialization and benchmarking in shock-driven turbulent mixing, J. Turbul. **14**, 46 (2013).

[37] I. W. Kokkinakis, D. Drikakis, D. L. Youngs, and R. J. R. Williams, Two-equation and multi-fluid turbulence models for Rayleigh-Taylor mixing, Int. J. Heat Fluid Flow **56**, 233 (2015).

[38] B. E. Morgan and M. E. Wickett, Three-equation model for the self-similar growth of Rayleigh-Taylor and Richtmyer-Meshkov instabilities, Phys. Rev. E **91**, 043002 (2015).

[39] J. D. Schwarzkopf, D. Livescu, J. R. Baltzer, R. A. Gore, and J. R. Ristorcelli, A two-length scale turbulence model for single-phase multi-fluid mixing, Flow Turbul. Combust. **96**, 1 (2016).

[40] B. E. Morgan and J. A. Greenough, Large-eddy and unsteady RANS simulations of a shock-accelerated heavy gas cylinder, Shock Waves **26**, 355 (2016).

[41] O. Schilling and N. J. Mueschke, Turbulent transport and mixing in transitional Rayleigh-Taylor unstable flow: *A priori* assessment of gradient-diffusion and similarity modeling, Phys. Rev. E **96**, 063111 (2017).

[42] B. E. Morgan, O. Schilling, and T. A. Hartland, Two-length-scale turbulence model for self-similar buoyancy-, shock-, and shear-driven mixing, Phys. Rev. E **97**, 013104 (2018).

[43] B. E. Morgan, B. J. Olson, W. J. Black, and J. A. McFarland, Large-eddy simulation and Reynolds-averaged Navier-Stokes modeling of a reacting Rayleigh-Taylor mixing layer in a spherical geometry, Phys. Rev. E **98**, 033111 (2018).

[44] A. Campos and B. E. Morgan, Direct numerical simulation and Reynolds-averaged Navier-Stokes modeling of the sudden viscous dissipation for multicomponent turbulence, Phys. Rev. E **99**, 063103 (2019).

[45] I. W. Kokkinakis, D. Drikakis, and D. L. Youngs, Modeling of Rayleigh-Taylor mixing using single-fluid models, Phys. Rev. E **99**, 013104 (2019).

[46] I. W. Kokkinakis, D. Drikakis, and D. L. Youngs, Two-equation and multi-fluid turbulence models for Richtmyer-Meshkov mixing, Phys. Fluids **32**, 074102 (2020).

[47] M. Xiao, Y. Zhang, and B. Tian, Unified prediction of reshocked Richtmyer-Meshkov mixing with K-L model, Phys. Fluids **32**, 032107 (2020).

[48] M. Xiao, Y. Zhang, and B. Tian, Modeling of turbulent mixing with an improved K-L model, Phys. Fluids **32**, 092104 (2020).

[49] Y. Zhang, Z. He, H. Xie, M.-J. Xiao, and B. Tian, Methodology

for determining coefficients of turbulent mixing model, J. Fluid Mech. **905**, A26 (2020).

[50] Y. Zhou, Rayleigh-Taylor and Richtmyer-Meshkov instability induced flow, turbulence, and mixing. I, Phys. Rep. **720**, 1 (2017).

[51] Y. Zhou, Rayleigh-Taylor and Richtmyer-Meshkov instability induced flow, turbulence, and mixing. II, Phys. Rep. **723**, 1 (2017).

[52] A. Llor and P. Bailly, A new turbulent two-field concept for modeling Rayleigh-Taylor, Richtmyer-Meshkov, and Kelvin-Helmholtz mixing layers, Laser Part. Beams **21**, 311 (2003).

[53] J. Griffond and O. Soulard, Evaluation of augmented RSM for interaction of homogeneous turbulent mixture with shock and rarefaction waves, J. Turbul. **15**, 569 (2014).

[54] G. L. Brown and A. Roshko, On density effects and large structure in turbulent mixing layers, J. Fluid Mech. **64**, 775 (1974).

[55] P. E. Dimotakis and G. L. Brown, The mixing layer at high Reynolds number: Large-structure dynamics and entrainment, J. Fluid Mech. **78**, 535 (1976).

[56] J. H. Bell and R. D. Mehta, Development of a two-stream mixing layer from tripped and untripped boundary layers, AIAA J. **28**, 2034 (1990).

[57] R. D. Moser and M. M. Rogers, Mixing transition and the cascade to small scales in a plane mixing layer, Phys. Fluids **3**, 1128 (1991).

[58] M. M. Rogers and R. D. Moser, The three-dimensional evolution of a plane mixing layer: The Kelvin-Helmholtz rollup, J. Fluid Mech. **243**, 183 (1992).

[59] R. D. Moser and M. M. Rogers, The three-dimensional evolution of a plane mixing layer: Pairing and transition to turbulence, J. Fluid Mech. **247**, 275 (1993).

[60] M. M. Rogers and R. D. Moser, Direct simulation of a self-similar turbulent mixing layer, Phys. Fluids **6**, 903 (1994).

[61] S. C. Collis, S. K. Lele, R. D. Moser, and M. M. Rogers, The evolution of a plane mixing layer with spanwise nonuniform forcing, Phys. Fluids **6**, 381 (1994).

[62] S. Laizet, S. Lardeau, and E. Lamballais, Direct numerical simulation of a mixing layer downstream a thick splitter plate, Phys. Fluids **22**, 015104 (2010).

[63] Q. Zhou, F. He, and M. Y. Shen, Direct numerical simulation of a spatially developing compressible plane mixing layer: Flow structures and mean flow properties, J. Fluid Mech. **711**, 437 (2012).

[64] D. Zhang, J. Tan, and X. Yao, Direct numerical simulation of spatially developing highly compressible mixing layer: Structural evolution and turbulent statistics, Phys. Fluids **31**, 036102 (2019).

[65] P. E. Dimotakis, Turbulent free shear layer mixing and combustion, High Speed Flight Propul. Syst. **137**, 265 (1991).

[66] P. S. Karasso and M. G. Mungal, Scalar mixing and reaction in plane liquid shear layers, J. Fluid Mech. **323**, 23 (1996).

[67] C. Pantano, S. Sarkar, and F. A. Williams, Mixing of a conserved scalar in a turbulent reacting shear layer, J. Fluid Mech. **481**, 291 (2003).

[68] A. Attili and F. Bisetti, Statistics and scaling of turbulence in a spatially developing mixing layer at $Re_\lambda = 250$, Phys. Fluids **24**, 035109 (2012).

[69] B. Wang, W. Wei, Y. Zhang, H. Zhang, and S. Xue, Passive scalar mixing in $M_c < 1$ planar shear layer flows, Comput. Fluids **123**, 32 (2015).

[70] D. D. Joseph, Fluid dynamics of two miscible liquids with diffusion and gradient stresses, Eur. J. Mech. B **9**, 565 (1990).

[71] W. H. Cabot and A. W. Cook, Reynolds number effects on Rayleigh-Taylor instability with possible implications for type Ia supernovae, Nat. Phys. **2**, 562 (2006).

[72] B. E. Morgan, B. J. Olson, J. E. White, and J. A. McFarland, Self-similarity of a Rayleigh-Taylor mixing layer at low Atwood number with a multimode initial perturbation, J. Turbul. **18**, 973 (2017).

[73] B. E. Morgan and W. J. Black, Parametric investigation of the transition to turbulence in Rayleigh-Taylor mixing, Physica D **402**, 132223 (2020).

[74] B. J. Olson, Large-eddy simulation of multi-material mixing and over-expanded nozzle flow, Ph.D. thesis, Stanford University, 2012.

[75] A. W. Cook, Artificial fluid properties for large-eddy simulation of compressible turbulent mixing, Phys. Fluids **19**, 055103 (2007).

[76] A. W. Cook, Enthalpy diffusion in multicomponent flows, Phys. Fluids **21**, 055109 (2009).

[77] B. J. Olson and J. Greenough, Large eddy simulation requirements for the Richtmyer-Meshkov instability, Phys. Fluids **26**, 044103 (2014).

[78] J. R. Ristorcelli, Exact statistical results for binary mixing and reaction in variable density turbulence, Phys. Fluids **29**, 020705 (2017).